

Unsupervised Learning of a Hierarchical Spiking Neural Network for Optical Flow Estimation: From Events to Global Motion Perception

Federico Paredes-Vallés , Kirk Y. W. Schepers , and Guido C. H. E. de Croon , Member, IEEE

Abstract—The combination of spiking neural networks and event-based vision sensors holds the potential of highly efficient and high-bandwidth optical flow estimation. This paper presents the first hierarchical spiking architecture in which motion (direction and speed) selectivity emerges in an unsupervised fashion from the raw stimuli generated with an event-based camera. A novel adaptive neuron model and spike-timing-dependent plasticity formulation are at the core of this neural network governing its spike-based processing and learning, respectively. After convergence, the neural architecture exhibits the main properties of biological visual motion systems, namely feature extraction and local and global motion perception. To assess the outcome of the learning, a shallow conventional artificial neural network is trained to map the activation traces of the penultimate layer to the optical flow visual observables of ventral flow. The proposed solution is validated for simulated event sequences with ground-truth measurements. Experimental results show that accurate estimates of these parameters can be obtained over a wide range of speeds.

Index Terms—Event-based computer vision, feature extraction, motion detection, neural nets, neuromorphic computing, STDP

1 INTRODUCTION

WHENEVER an animal endowed with a visual system navigates through an environment, turns its gaze, or simply observes a moving object from a resting state, motion patterns are perceivable at the retina level as spatiotemporal variations of brightness [1]. These patterns of apparent motion, formally referred to as *optical flow* [2], are a crucial source of information for these animals to estimate their ego-motion and to have a better understanding of the visual scene. A great example of the efficacy of these cues in nature is in flying insects. They are believed to heavily rely on these visual cues to perform high-speed maneuvers such as horizontal translation or landing [3], [4], [5].

Considering their size and weight limitations, insects are a clear indicator of the efficiency, robustness, and low latency of the optical flow estimation conducted by biological systems. The ability to reliably mimic this procedure would have a significant impact on the field of micro-robotics due to the limited computational capacity of their onboard processors. As an example, Micro Air Vehicles (MAVs), such as the 20-gram DelFly Explorer [6], could benefit from a bio-inspired visual motion estimation for high-speed autonomous navigation in cluttered environments.

Biological visual systems receive their input from photoreceptors in the retina. These light-sensitive neurons ab-

sorb and convert incoming light into electrical signals which serve as input to the so-called ganglion cells. The activity of these neurons consists of temporal sequences of discrete *spikes* (voltage pulses) that are sent to large networks of interconnected cells for motion estimation, among other tasks. Since it is spike-driven, these biological architectures are characterized by a sparse, asynchronous, and massively parallelized computation. Further, they are seen to adapt their topology, i.e. connectivity pattern, in response to visual experience [7]. This adaptation, or *learning* mechanism, allows them to operate robustly in different environments under a wide range of lighting conditions.

In contrast, the working principle of the majority of cameras used for artificial visual perception is categorized as *frame-based*: data is obtained by measuring the brightness levels of a pixel array at fixed time intervals. Although convenient for some computer vision applications, these sensors are inefficient for the task of motion estimation as the frame rate is independent of the dynamics of the visual scene. Additionally, due to the limited temporal resolution of these sensors, rapidly moving objects may introduce motion blur, limiting the accuracy of optical flow estimation.

However, not all artificial systems rely on conventional frame-based cameras for visual motion estimation. Inspired by biological retinas, several *event-based* sensors have recently been presented [8], [9], [10]. Similar to ganglion cells, each of the elements of the pixel array reacts asynchronously to brightness changes in its corresponding receptive field by generating *events*. Microsecond resolution, latencies in this order of magnitude, wide dynamic range, and low power consumption make these sensors an ideal choice for visual perception [11], [12], [13].

Regardless of the vision sensor, the estimation of optical flow by artificial systems is normally performed algorithmi-

• Federico Paredes-Vallés, Kirk Y. W. Schepers, and Guido C. H. E. de Croon are with the Department of Control and Simulation (Micro Air Vehicle Laboratory), Faculty of Aerospace Engineering, Delft University of Technology, Kluyverweg 1, 2629 HS Delft, The Netherlands.

E-mail: {f.paredesvalles, k.y.w.schepers, g.c.h.e.decroon}@tudelft.nl

Manuscript received 00 Aaa. 0000; revised 00 Aaa. 0000; accepted 00 Aaa 0000. Date of publication 00 Aaa 0000; date of current version 00 AA 0000. Recommended for acceptance by X. XXXXX. For information on obtaining reprints of this article, please send e-mail to: reprints@ieee.org, and reference the Digital Object Identifier below. Digital Object Identifier no. 00.0000/TPAMI.0000.0000000

cally, with solutions that are built on simplifying assumptions that make this problem tractable [14], [15]. In spite of this, the recent progress in parallel computing hardware has enabled artificial visual perception to be addressed from a more bio-inspired perspective: Artificial Neural Networks (ANNs). Similar to biological architectures, ANNs consist of large sets of artificial neurons whose interconnections can be optimized for the task at hand. However, despite the high accuracy reported [16], there is still a fundamental difference: the underlying data transfer mechanism of ANNs is based on a continuous stream of information rather than on trains of asynchronous discrete spikes. As a consequence, these architectures are often computationally expensive.

Taking further inspiration from nature, Spiking Neural Networks (SNNs) have been proposed as a new generation of ANNs [17]. As the name suggests, the computation carried out by these bio-realistic neural models is asynchronous and spike-based, which makes them a suitable processing framework for the sparse data generated by event-based vision sensors [18]. Moreover, SNNs can benefit from an efficient real-time implementation in *neuromorphic hardware*, such as IBM’s TrueNorth chip [19] or Intel’s Loihi processor [20]. Despite these promising characteristics, the spiking nature of these networks limits the application of the successful gradient-based optimization algorithms normally employed in ANNs. Instead, learning in SNNs is dominated by Spike-Timing-Dependent Plasticity (STDP) [21], [22], a biologically plausible protocol that adapts the strength of a connection between two neurons based on their correlated activity. STDP has been successfully applied to relatively simple image classification tasks [23], [24], [25]. However, until now, no study has discussed the use of this learning rule for the estimation of event-based optical flow.

This paper contains *three main contributions*. First, a novel adaptive mechanism for the Leaky Integrate-and-Fire (LIF) spiking neuron model [26] is introduced. This adaptation extends the applicability of this model to the rapidly varying input statistics of a moving event-based vision sensor. Second, a novel, inherently-stable STDP implementation is proposed. With this learning rule, the strength of neural connections is naturally constrained without the need for the ad-hoc mechanisms used by most of the existing formulations. Third, the proposed neuron model and STDP rule are combined in a bio-inspired hierarchical SNN architecture that, after learning, resembles the main functionalities of biological visual systems: feature extraction and local and global motion perception. To the best of the authors’ knowledge, this paper shows, for the first time, that neural selectivity to the local and global motion of input stimuli can emerge from visual experience in a biologically plausible unsupervised fashion.

The rest of the paper is structured as follows. Section 2 provides background information concerning event-based vision, SNNs, and optical flow estimation. The foundations of the spike-based processing and learning of the proposed SNN are detailed in Sections 3 and 4, respectively. Thereafter, network architecture is described and evaluated in Section 5. Lastly, Section 6 introduces an ANN-based readout mechanism to obtain continuous values as estimates of optical flow visual observables from the activation traces of the SNN.

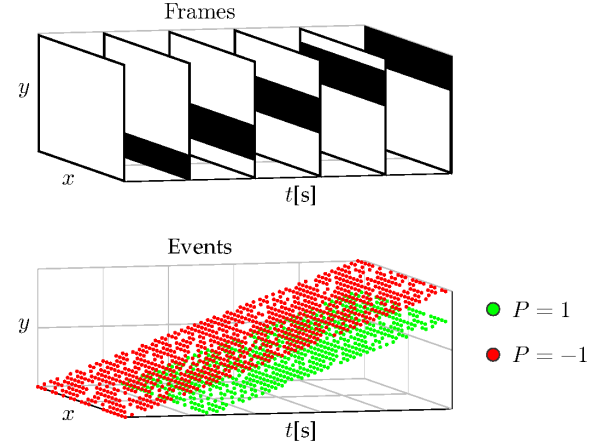


Fig. 1: Comparison of the output of frame- and event-based vision sensors under the stimulus of a black horizontal bar moving upward over a homogeneous white background. While frames are basically two-dimensional snapshots of the visual scene, events are spatiotemporal sparse points tracking the leading and trailing edges of the bar.

2 BACKGROUND INFORMATION

2.1 Event-Based Vision Sensors

Inspired by biological retinas, each of the pixels of an event-based vision sensor reacts asynchronously to local changes in brightness by generating discrete temporal events. Specifically, the generation of an event is triggered whenever the logarithmic change of the image intensity $I(x, y, t)$ exceeds a predefined threshold C such that $|\Delta \log(I(x, y, t))| > C$ [8]. This variation is computed with respect to a reference brightness level set by the last occurring event at that pixel.

Each event encodes information about the timestamp t in which it was generated, the corresponding (x, y) location in the pixel array, and the polarity $P \in \{-1, 1\}$ of the intensity change. This communication protocol is formally referred to as Address-Event Representation (AER). A visual comparison of the output of frame- and event-based sensors under the same stimulus is illustrated in Fig. 1.

The event-based camera employed in this work is the Dynamic Vision Sensor (DVS), more specifically, the DVS128. This device features a 128×128 pixel array characterized by a temporal resolution of $1 \mu\text{s}$, a latency of $12 \mu\text{s}$, an intrascene dynamic range of 120 dB , and an average power consumption of 23 mW [8]. In this work, the streams of DVS events are generated with the DVS simulator [27], rather than with the actual sensor. This simulator renders intensity images from a three-dimensional virtual scene at a high rate (1000 Hz), and estimates events by linearly interpolating logarithmic brightness levels between frames. The use of virtual scenes facilitates the acquisition of ground truth measurements, which are essential for the performance assessment of motion estimation approaches.

2.2 Spiking Neural Networks

Models of spiking neurons: In biological networks, neural communication consists in the exchange of voltage pulses [17]. For the reproduction of this asynchronous and spike-based mechanism in SNNs, multiple models of spiking neurons have been presented at various levels of abstract-

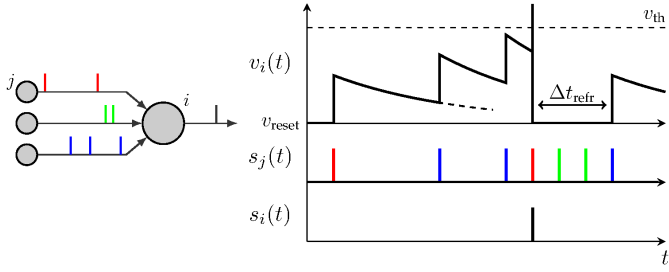


Fig. 2: A model of a LIF neuron. The graphic (right) shows the temporal course of the membrane potential $v_i(t)$ of the i th neuron (left), driven by a sample presynaptic spike train $s_i(t)$ from three input neurons $j = 1, 2, 3$. Spikes are depicted as vertical bars at the time at which they are received (if presynaptic) or emitted (if postsynaptic). In this schematic, the reset v_{reset} and resting v_{rest} potentials are equal in magnitude.

tion. Biophysical formulations lead to accurate representations of neural dynamics [28], however, their complexity limits their use in large-scale networks. Alternatively, phenomenological formulations offer a compromise between computational load and biological realism. The most used models are the aforementioned LIF [26], the Izhikevich [29], and the Spike Response Model [30].

From a conceptual perspective, the majority of these models share some fundamental principles and definitions. The junction of two neurons is called *synapse*; and relative to these cells, the transmitting neuron is labeled as *presynaptic*, while the receiving as *postsynaptic*. Each spiking neuron, as processing unit, is characterized by an internal state variable, known as *membrane potential* $v(t)$, which temporally integrates presynaptic spikes over time. If the arrival of a spike leads to an increase (decrease) in $v(t)$, then the spike is said to have an *excitatory (inhibitory)* effect on the neuron. $v(t)$ decays to a resting potential v_{rest} in case no input is received. Lastly, a postsynaptic spike is triggered whenever $v(t)$ crosses the *firing threshold* v_{th} . Afterwards, the neuron resets its membrane potential to v_{reset} , and enters in a *refractory period* Δt_{refr} during which new incoming spikes have negligible effect on $v(t)$. Fig. 2 illustrates these concepts for the case of a LIF neuron [26].

Synaptic plasticity: Defined as the ability to modify the *efficacy* (weight) of neural connections, *synaptic plasticity* is the basic mechanism underlying learning in biological networks [31]. These architectures are seen to rely on different learning paradigms depending on their duty [32]. For instance, information encoding in biological visual systems is established in an unsupervised fashion, while reinforcement and supervised learning are employed for tasks such as decision making and motor control. Accordingly, various forms of synaptic plasticity have been proposed for SNNs.

In the context of SNNs, unsupervised learning is generally referred to as Hebbian learning, since plasticity rules from this paradigm are based on Hebb's postulate: "*cells that fire together, wire together*" [33]. In essence, these methods adapt the efficacy of a connection based on the correlated activity of pre- and postsynaptic cells. Among others, the biologically plausible STDP protocol [21], [22] is, by far, the most popular Hebbian rule for SNNs [34]. With STDP, the repeated arrival of presynaptic spikes to a neuron shortly before it fires leads to synaptic strengthening, also known as Long-Term Potentiation (LTP); whereas if the arrival

occurs shortly after the postsynaptic spike, synapses are weakened through Long-Term Depression (LTD). Therefore, the change of efficacy ΔW is normally expressed as a function of the relative timing between these two events. STDP formulations exclusively dependent on this parameter are referred to as *additive* rules [35]. These models, despite their success in pattern recognition problems [23], [24], [25], [36], are inherently unstable and require the use of constraints for the synaptic weights, thus resulting in bimodal distributions [37]. On the other hand, *multiplicative* STDP rules incorporate the current efficacy value in the computation of ΔW in an inversely proportional manner. As shown in [38], [39], this additional dependency leads to stable unimodal weight distributions. However, the stability of these approaches results from a complex temporal LTP-LTD balance, and it is not theoretically guaranteed.

Several lines of research can be distinguished regarding the use of supervised learning in SNNs, being the most promising based on the well-known error backpropagation algorithm. Firstly, numerous adaptations to the discontinuous dynamics of SNNs have been proposed for learning temporally precise spike patterns [40], [41]; but no vision-based applications have been reported. Alternatively, due to the popularity of this method in ANNs, SNNs normally rely on transferring optimization results from their non-spiking counterparts [42], [43]. Even though similar accuracy levels are obtained more efficiently, information is no longer encoded in the precise spike timing but rather in the neural firing rate, which differs from biological visual systems [44].

With respect to reinforcement learning in SNNs, various models have been presented, the majority of which consist in the modulation of STDP with a reward function [45], [46]. However, applications of this paradigm are mainly focused on neuroscience research [47], [48], besides several goal-directed navigation problems [49] and the digit-recognition application recently presented in [50].

2.3 Optical Flow

This paper uses the definition of optical flow from [13]. Here, the derivation of this optical flow is made in the camera frame centered at the focal point of the event-based vision sensor and pixel coordinates are denoted by (x, y) . Position is defined by the Cartesian coordinates (X_c, Y_c, Z_c) , with (U_c, V_c, W_c) as the corresponding velocity components. The subscript C here denotes that this coordinate frame is camera-fixed with the Z_c axis aligned with the lens pointing away from the camera, and the X_c axis towards the right when looking through the lens. The orientation of vision sensor from with respect to the world frame is described by the Euler angles ϕ , θ , and ψ , denoting roll, pitch, and yaw, respectively.

Using the pinhole camera model from [51], the ventral flow components (ω_x, ω_y) , and the flow field divergence D are represented as follows:

$$\omega_x = -\frac{U_c}{Z_0}, \quad \omega_y = -\frac{V_c}{Z_0}, \quad D = 2\frac{W_c}{Z_0} \quad (1)$$

where Z_0 is defined as the distance to the surface along the optical axis of the sensor.

2.4 Event-based Optical Flow Estimation

The recent introduction of the DVS and other retinomorphic vision sensors has precipitated the development of several novel approaches to event-based optical flow estimation. Depending on their working principle, these solutions are divided into algorithmic and neural methods.

Gradient-, plane-fitting-, and various frequency-based approaches set the basis of the algorithmic state-of-the-art. These techniques compute sparse optical flow estimates for each newly detected event based on its polarity-specific spatiotemporal neighborhood. Firstly, an adaptation of the Lucas-Kanade algorithm [52] was presented in [53], and reformulated in [54]. Secondly, the method proposed in [15] extracts optical flow information by computing the gradients of a local plane fitted to represent a spatiotemporal surface of events. This plane-fitting algorithm is further explored in [13], where its applicability is extended to a wider range of velocities through an adaptive temporal window. Lastly, multiple adaptations of the bio-inspired frequency-based methods have been introduced [54], [55]. Although relying on the same principle as their frame-based counterparts, the event-driven computations allow the implementation in neuromorphic hardware [56].

The estimation of event-based optical flow with neural models is dominated, almost in its entirety, by SNNs. In [57], the authors propose an architecture in which motion selectivity results from the synaptic connections of a bursting neuron to two neighboring photoreceptors, one excitatory and the other inhibitory. If the edge is detected first by the excitatory cell, spikes are emitted at a fixed rate until the inhibitory pulse is received. Otherwise, the neuron remains inactive. Optical flow is consequently encoded in the burst length and in the relative orientation of the photoreceptors.

In contrast, the SNNs presented in [58], [59] extract motion information through synaptic delays and spiking neurons acting as coincidence detectors. A simple spike-based adaptation of the Reichardt model [60] is introduced in [58] to show the potential of this approach. This idea is explored in more detail in [59], in which the authors propose the convolution of event sequences with a bank of spatiotemporally-oriented filters, each of which is comprised of non-plastic synapses with equal efficacies, but with delays tuned to capture a particular direction and speed. Similarly to frequency-based methods [14], these filters compute a confidence measure, encoded in the neural activity, rather than the optical flow components. Additionally, this solution employs a second spike-based pooling layer for mitigating the effect of the aperture problem [61].

Whether, and how, direction and speed selectivity emerge in biological networks from visual experience still remains an open question. Some initial work by [62], [63], [64] shows that robust local direction selectivity arises in neural maps through STDP if, apart from presynaptic feed-forward connections, neurons receive spikes from cells in their spatial neighborhood through plastic synapses with distance-dependent transmission delays. However, no study has assessed the speed selectivity of these cells, which is crucial for optical flow estimation.

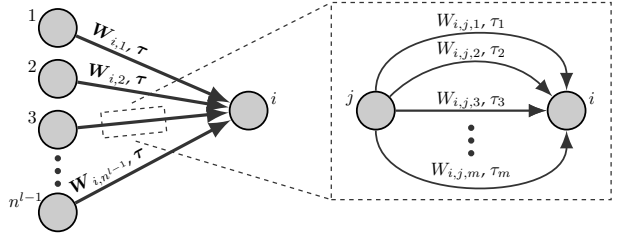


Fig. 3: Schematic of the feedforward connectivity between neurons from two adjacent layers (left). These connections can be considered as being *multisynaptic* (right), each one having its own efficacy, transmission delay, and trace.

3 ADAPTIVE SPIKING NEURON MODEL

Let $j = 1, 2, \dots, n^{l-1}$ denote a group of presynaptic neurons, from layer $l-1$, fully connected in a feedforward fashion to a set of postsynaptic cells $i = 1, 2, \dots, n^l$, from layer l . As depicted in Fig. 3, these neural connections can be considered as *multisynaptic*, i.e. the link between two cells is not restricted to a single synapse, but several can coexist. In this implementation, the number of multisynaptic connections, denoted by m , is layer-specific. Based on this, layer connectivity is characterized by two main elements: a weight matrix $\mathbf{W} \in \mathbb{R}^{n^l \times n^{l-1} \times m}$ and a delay vector $\boldsymbol{\tau} \in \mathbb{R}^m$. From the definition of \mathbf{W} , each connection has its own independent synaptic efficacy value. On the other hand, $\boldsymbol{\tau}$ determines the different transmission delays of a multisynaptic group of connections.

Apart from \mathbf{W} and $\boldsymbol{\tau}$, each synapse keeps track of an additional parameter that captures the recent history of spikes transmitted. Referred to as the *presynaptic trace* [65], and defined as $\mathbf{X} \in \mathbb{R}^{n^l \times n^{l-1} \times m}$, its dynamics is given by:

$$\lambda_X \frac{dX_{i,j,d}(t)}{dt} = -X_{i,j,d}(t) + \alpha s_j^{l-1}(t - \tau_d) \quad (2)$$

where λ_X is the time constant of the system, α is a scaling factor, and $s^l(t) \in \mathbb{R}^{n^l}$ denotes the (binary) record of neural activity, or *spike train*, of cells from layer l . Note that $d = 1, 2, \dots, m$ serves to refer both to connections within a multisynaptic group and their corresponding delays.

From Eq. (2), whenever a spike arrives at a postsynaptic neuron i via a synapse with transmission delay τ_d , the corresponding presynaptic trace $X_{i,j,d}(t)$ increases by a factor of α . In case no spike is received, the trace decays exponentially towards zero according to λ_X .

The LIF model is the most widely used spiking neural model in literature. This is due to its main assumption that in SNNs, information is not encoded in the spike amplitude, but rather in the firing time. Consequently, neural activity is reduced to discrete and binary temporal events, thus ensuring computational tractability. The spiking neural model used in this paper is a modified LIF model, defined as:

$$\lambda_v \frac{dv_i^l(t)}{dt} = -(v_i^l(t) - v_{\text{rest}}) + i_i^l(t) \quad (3)$$

$$i_i^l(t) = \sum_{j=1}^{n^{l-1}} \sum_{d=1}^m (W_{i,j,d} s_j^{l-1}(t - \tau_d) - X_{i,j,d}(t)) \quad (4)$$

where λ_v denotes the time constant of the membrane potential, and $i_i^l(t)$ is the so-called *forcing function* of the system.

From Eqs. (3) and (4), the membrane potential $v_i^l(t)$ of a neuron evolves over time by integrating scaled presynaptic spikes from its input synapses, similarly to the conventional LIF model [26]. Whenever $v_i^l(t)$ reaches (or surpasses) the firing threshold v_{th} , a postsynaptic spike is generated, i.e. $s_i^l(t) = 1$, and $v_i^l(t)$ is reset to v_{reset} . In addition, the neuron enters in a refractory period Δt_{refr} during which presynaptic spikes have no effect on $v_i^l(t)$ to ensure the temporal separation of postsynaptic pulses. In case no spike is fired at time t , this is reflected in the neuron's spike train as $s_i^l(t) = 0$.

Unlike traditional LIF [26], the forcing function $i^l(t)$ of our neuron model includes an additional term, further referred to as the *homeostasis* parameter. This is used to adapt the neural response to the varying input statistics—in particular, to the input firing rate—using the presynaptic trace \mathbf{X} as an *excitability* indicator. This term is inspired by the internal regulatory mechanisms of biological organisms [66]. Inferring from Eq. (4), this parameter acts, in essence, as an inhibitory penalty in the update rule of $v_i^l(t)$. A postsynaptic neuron connected to a group of highly-active presynaptic cells is said to have low excitability due to its relatively high \mathbf{X} . For this neuron to fire, it needs to receive a large number of presynaptic spikes shortly separated in time. Conversely, the same cell connected to poorly-active neurons is highly excitable; and thus, the firing threshold v_{th} can still be reached despite the considerably larger time difference between input spikes. Note that, to get the desired neural adaptation, the scaling factor α , from Eq. (2), needs to be selected in accordance with the neural parameters, mainly v_{th} and the range of possible \mathbf{W} values.

When dealing with an event-based camera as source of input spikes, the firing rate of the sensor is not only correlated to the appearance of features from the visual scene, but also to their optical flow and the sensitivity settings of the camera. Slow apparent motion leads to successive events being more distant in time than those captured from fast motion. Consequently, if these events are to be processed with a network of spiking neurons, a homeostasis mechanism is required to ensure that similar features are detected regardless of the encoding spike rate.

Other approaches to homeostasis have been presented in the literature, such as threshold balancing [67] or weight scaling [38]. However, these methods use postsynaptic

spikes to adjust the homeostatic inhibition through an adaptive mechanism. With this neural feedback, there is a delay in adjusting the excitability of the neurons. These approaches are therefore less suitable for the rapidly varying statistics of the data generated by a moving event-based vision sensor.

4 STABLE STDP LEARNING RULE

In this work, we propose a novel multiplicative STDP implementation that, contrary to the state-of-the-art of this learning protocol, is inherently stable by combining the weight-dependent exponential rule from [39] with presynaptic trace information. Whenever a neuron i fires a spike, the efficacy of its presynaptic connections is updated as follows:

$$\Delta W_{i,j,d} = \eta(\text{LTP} + \text{LTD}) \quad (5)$$

$$\begin{aligned} \text{LTP} &= \text{LTP}_W \cdot \text{LTP}_{\hat{X}}, & \text{LTD} &= \text{LTD}_W \cdot \text{LTD}_{\hat{X}} \\ \text{LTP}_W &= e^{-(W_{i,j,d} - w_{\text{init}})}, & \text{LTD}_W &= -e^{(W_{i,j,d} - w_{\text{init}})} \\ \text{LTP}_{\hat{X}} &= e^{\hat{X}_{i,j,d}(t)} - a, & \text{LTD}_{\hat{X}} &= e^{(1 - \hat{X}_{i,j,d}(t))} - a \end{aligned} \quad (6)$$

where η is the learning rate of the rule, w_{init} refers to the initialization weight of all synapses at the beginning of the learning process, and $\hat{X}_i \in [0, 1]$ denotes the presynaptic traces of neuron i normalized to the current maximum at the moment of firing. Further, for stability, $\eta > 0$ and $a < 1$ regardless of the value of w_{init} (see Appendix).

From Eqs. (5) and (6), the weight update ΔW_i results from the linear combination of the output of two non-mutually exclusive processes: LTP, for strengthening, and LTD, for weakening synaptic connections. Both of these processes are dependent on the weights (LTP_W , LTD_W) and normalized traces ($\text{LTP}_{\hat{X}}$, $\text{LTD}_{\hat{X}}$) of the synapses under analysis. On the one hand, the weight dependency of our learning rule takes inspiration from the STDP formulation presented in [39]. LTP_W and LTD_W are inversely proportional to W_i in an exponential fashion, and are centered around w_{init} (see Fig. 4, left). Consequently, the effect of LTP_W decreases (increases) the larger (smaller) a synaptic weight is in comparison to w_{init} . The opposite relation holds true for LTD_W . On the other hand, rather than relying on the precise spike timing [39], our rule employs normalized

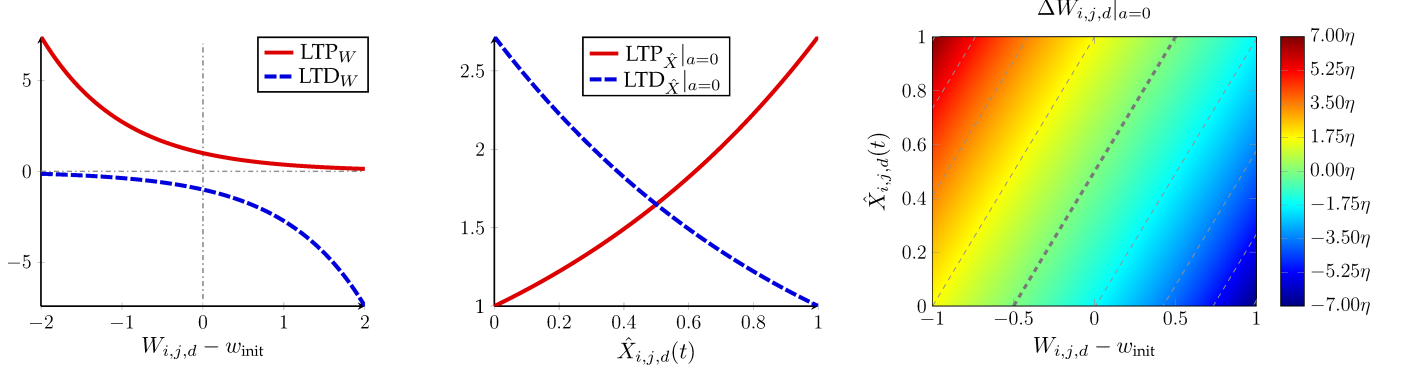


Fig. 4: Illustration of the novel multiplicative STDP rule proposed in this work. The weight update (right) results from the linear combination of the non-exclusive LTP and LTD processes. These, in turn, are characterized by symmetrical dependencies on the synaptic weights (left) and normalized presynaptic traces (center). Note that, in the schematic of the weight update (right), the weight axis is limited to the $[-1, 1]$ range only for the purpose of a better visualization of the equilibrium weights (dashed thick line) for $a = 0$.

presynaptic trace information as a measure of the relevance of a particular connection to the postsynaptic spike triggering the update. The higher (lower) the value of $\hat{X}_{i,j,d}(t)$, the larger (smaller) the effect of LTP \hat{X} , and vice versa for LTD \hat{X} (see Fig. 4, center).

With this formulation, a weight is established for each value of $\hat{X}_{i,j,d}(t)$ through a stable equilibrium of contributions of LTP and LTD on ΔW_i (see Fig. 4, right). The parameter a has control over this non-linear mapping through the steepness of LTP \hat{X} and LTD \hat{X} in $\hat{X}_i \in [0, 1]$. The higher (lower) the value of a —below the aforementioned stability limit—, the wider (narrower) the distribution of synaptic weights after convergence. As such, no additional mechanism is required for preventing weights from vanishing or exploding. Synapses characterized by weights that are higher (lower) than their corresponding equilibrium state are consistently depressed (potentiated) until synapse-specific stability is achieved.

To track the convergence of the learning process, we propose the use of the following mean square error criterion:

$$\mathcal{L}_i = \frac{1}{n^{l-1}m} \sum_{j=1}^{n^{l-1}} \sum_{d=1}^m (\hat{X}_{i,j,d}(t) - \hat{W}_{i,j,d})^2 \quad (7)$$

where $\hat{W}_i \in [0, 1]$ denotes the presynaptic weights of neuron i after an update, normalized to the current maximum value. As the learning progresses, the moving average of \mathcal{L}_i converges to a (close-to-zero) equilibrium state. In this work, we stop synaptic plasticity using a fixed threshold on this parameter, denoted by \mathcal{L}_{th} .

Hereafter, we utilize this modified STDP rule and will simply refer to it as STDP.

4.1 Local inter-lateral competition

For neurons to learn distinct features from the input data through STDP, this learning rule needs to be combined with what is known as a Winner-Take-All (WTA) mechanism [68]. This form of competition implies that, when a neuron fires a spike and updates its presynaptic weights according to Eqs. (5) and (6), the rest of postsynaptic cells (from the same layer) locally connected to the same input neurons get inhibited. As a result, these cells are prevented from triggering STDP while the neuron that fired first, i.e. the *winner*, remains in the refractory period.

Instead of relying on non-plastic synapses transmitting inhibitory spikes with a certain delay, our implementation assumes that the internal dynamics of these neurons are intercorrelated. Whenever the winner resets its membrane potential and enters in the refractory period, neurons affected by the WTA mechanism do the same immediately afterwards. In case multiple neurons fire simultaneously, the cell with the highest membrane potential has preference for triggering the weight update. Further, the postsynaptic spikes from the other firing neurons are not considered. To ensure coherence between the training and inference phases of our proposed SNN, layers trained with STDP maintain the WTA mechanism after the learning process.

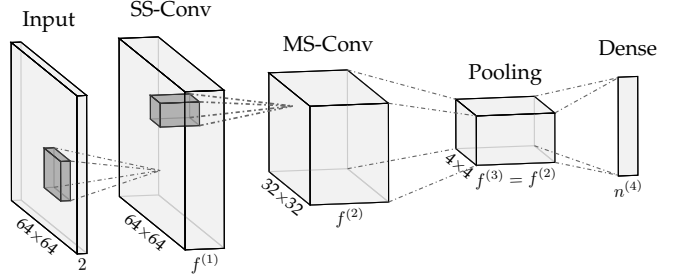


Fig. 5: Overview of the feedforward SNN architecture.

5 SPIKING NEURAL NETWORK ARCHITECTURE FOR MOTION PERCEPTION

To extract a robust measure of motion from the raw camera input is not a trivial task. For this we employed a multi-layer SNN illustrated in Fig. 5, each layer with a unique goal. The Input layer is the first stage of the network that encodes event-based sensor data in a compatible format for the rest of the architecture. Secondly, visual feature extraction is conducted with the single-synaptic convolutional layer (SS-Conv). Third, the local motion of these features are identified through a multi-synaptic convolutional layer (MS-Conv). Lastly, a Pooling and a Dense, i.e. fully-connected, layer lead to the emergence of sensitivity to the global motion of the visual scene in individual neurons.

The spike-based neural computation is based on the adaptive neuron model introduced in Section 3. The membrane potential of all non-input neurons evolves according to Eq. (3), and the definition of the model forcing function $i^l(t)$ varies depending on the connectivity scheme of each layer, but maintaining the foundations of Eq. (4). In this work, the resting potential v_{rest} is considered null, and the refractory period is set to $\Delta_{\text{refr}} = 3.0$ ms. Additionally, for the simulation of the SNN, time is discretized in temporal units of length Δt_{sim} , in which neurons are only allowed to fire once.

Concerning learning, the SNN is trained in a *layer-by-layer* fashion using the unsupervised STDP rule presented in Section 4. Regardless of the layer type, the parameter a from Eq. (6) is set to 0, and the initialization weight w_{init} to 0.5. As shown in Fig. 4 (right), this leads to weight distributions that, after convergence, are naturally constrained in the range $W \in [0, 1]$. In addition, the learning rate η is set to 2.5×10^{-4} , and the convergence threshold \mathcal{L}_{th} to 5.0×10^{-2} . Throughout the learning phase, 150-ms event sequences from a training dataset are presented sequentially at random following a uniform distribution.

For the generation of the visual stimuli employed in this section, the simulated DVS [27] is moved in straight lines at different constant speeds, and at an altitude of 0.5 m with respect to a (virtual) textured planar surface, towards which it is facing. During motion, we force the Euler angles ϕ and θ to remain null so as to ensure the perpendicularity between sensor and surface. Fig. 6 shows the two different textures used in this work. The main experiments are based on the checkerboard pattern. This texture provides high contrast and clear edges which generates a reliable and repeatable quality of data from the event camera. This is useful for our later analysis of the optical flow estimation. On the

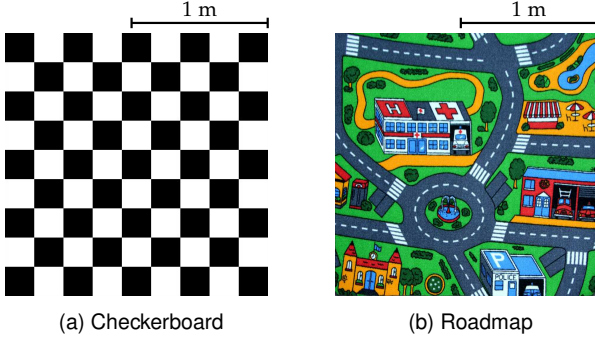


Fig. 6: Texture patterns of the planar surface towards which the vision sensor is facing during motion.

other hand, the roadmap pattern is largely characterized by unstructured and low-contrast visual features leading to noisy event sequences. It is used in the evaluation of the SS-Conv layer to show the generalizability of this approach to more realistic scenarios.

The simulation of the proposed SNN architecture is conducted using the *cuda-snn*¹ framework. This simulator, built in its entirety for this research, is written in the C++ programming language, and benefits from the NVIDIA CUDA libraries for efficient parallel computation.

5.1 Input Layer

The role of this first stage in the neural architecture is to encode the arriving sequences of DVS events into a format that is compatible with subsequent layers of the network. This layer can be understood as to be comprised of spiking neurons with no internal dynamics, whose neural activity is determined by event arrival. Neurons are arranged in two-dimensional *neural maps*, one per polarity, resembling the grid-like topology of the vision sensor. Depending on the spatial resolution of these maps, each neuron is assigned with the polarity-specific events of one or multiple DVS pixels with no overlap.

In the experiments presented in this section, the 128×128 DVS pixel array is downsampled to a spatial resolution of 64×64 input neurons for computational efficiency purposes. Contrary to the microsecond resolution of the DVS, Δt_{sim} is set to 1.0 ms, which is the timescale of the current state-of-the-art of neuromorphic computing devices [19], [20].

5.2 SS-Conv Layer: Feature Extraction

The single-synaptic convolutional layer is a spiking adaptation of the well-known convolutional layers in conventional ANNs. The goal of this layer is to extract visual features from the input. Neurons in the SS-Conv layer are retinotopically arranged in $k = 1, 2, \dots, f^l$ two-dimensional maps. Each of these neurons receives spikes from presynaptic cells within a specific spatial receptive field, of size r^{l-1} , in all maps of the previous layer. This sparse connectivity is characterized by a set of excitatory synaptic weights, formally referred to as a *convolutional kernel* \mathbf{W}_k , that is equal for all neurons belonging to the same map. Consequently, this form of *weight sharing* ensures that, within a map, neurons

are selective to the same input feature but at different spatial locations. This layer maintains the input (spatial) dimensionality through a convolutional stride of one pixel and a zero-padding mechanism.

Let a postsynaptic neuron i from the map k be characterized by the convolutional kernel $\mathbf{W}_k \in \mathbb{R}^{r^{l-1} \times f^{l-1}}$, the presynaptic trace $\mathbf{X}_i \in \mathbb{R}^{r^{l-1} \times f^{l-1}}$, and the spike train $s_{i,k}(t)$. Further, let $\mathbf{N}_{i,k}$ refer to the map-specific direct neural neighborhood of the cell, including itself. Then, considering neural connections as single-synaptic with transmission delay τ , the forcing function driving the internal dynamics of neurons in this layer is defined as follows:

$$i_{i,k}^l(t) = \sum_{j=1}^{r^{l-1}} \sum_{ch=1}^{f^{l-1}} W_{j, ch, k} s_{j, ch}^{l-1}(t - \tau) - \max_{\forall b \in \mathbf{N}_{i,k}} \sum_{j=1}^{r^{l-1}} \sum_{ch=1}^{f^{l-1}} X_{b, j, ch}(t) \quad (8)$$

Apart from the sparse connectivity, the only difference between this expression and the fully-connected formulation, i.e. Eq. (3), is in the homeostasis parameter. When arranged retinotopically, the neurons dynamics do not only depend on their own presynaptic trace \mathbf{X}_i , but also on the synaptic traces characterizing their direct spatial neural neighborhood $\mathbf{N}_{i,k}$. By using the maximum trace, neurons are prevented from specializing to the leading edge of moving visual features, rather than to the features themselves.

An augmentation of the proposed STDP rule is also required to handle the fact that multiple updates can be generated simultaneously in different spacial locations of the same map. Since these neurons share convolutional kernel, $\Delta \mathbf{W}_k$ is computed through synapse-specific averages of the local contributions. Additionally, due to the high overlap of presynaptic receptive fields, the WTA inhibitory mechanism described in Section 4.1 is expanded to cells within a small neighborhood of the firing neurons, regardless of the neural map. Note that, after learning, only the neuron-specific competition is maintained.

To qualitatively evaluate the performance of the SS-Conv layer when exposed to a complex input, we used the roadmap texture from Fig. 6b. In this experiment, the (constant) ventral flow components of the stimuli, ω_x and ω_y , ranged between 0.5 and 3.0 s^{-1} , in absolute terms. Further, neural parameters were empirically set to $v_{\text{th}} = 1.0$, $\lambda_v = \lambda_X = 5.0$ ms, $\tau = 1.0$ ms, and $\alpha = 0.4$ shows the appearance of sixteen 7×7 convolutional kernels learned through the proposed STDP rule under these conditions.

With this kernel scale, our STDP implementation led to the successful identification of edges at different orientations within the receptive field, and with the two combinations of event polarity. A point to remark is the fact that, despite the WTA mechanism, some features were learned by multiple kernels instead of being specific to just one. This is an indicator that, first, the unsupervised nature of STDP prioritizes frequent features over other, more complex, that can still be useful for motion perception; and second and consequently, sixteen is an unnecessarily large number of kernels for this spatial scale and roadmap dataset.

Fig. 7b illustrates the need for the homeostasis parameter as detailed in Eq. (8), when dealing with retinotopically-

1. Source code to be released in <https://github.com/tudelft/>

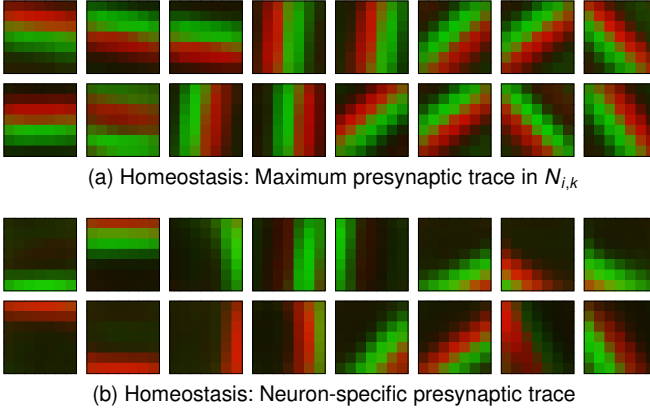


Fig. 7: 7×7 SS-Conv kernels learned from the roadmap texture. Synaptic strength is encoded in color brightness: green for input neurons with positive event polarity, and red for negative. Results are shown for the homeostasis formulations in Eq. (8) (top) and Eq. (4) (bottom).

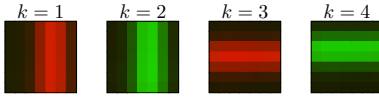


Fig. 8: 7×7 SS-Conv kernels learned from the checkerboard texture.

arranged neurons. As shown, when the formulation in Eq. (4) is employed instead, convolutional kernels specialize to the leading edge of moving features, and hence most of these kernels are characterized by more ambiguous synaptic configurations in which the strong synapses are mainly located on the receptive field borders. Because of this selectivity, a larger number of kernels is required for the extraction of the same features than with Eq. (8).

To simplify the analysis of later layers, we repeated the STDP using the checkerboard texture from Fig. 6a. The DVS orientation was fixed with respect to the checkerboard pattern so that only vertical and horizontal edges of both (event) polarities were perceived, and the stimuli were characterized by pure horizontal and vertical motion of $\{|\omega_x|, |\omega_y|\} \in [0.2, 4.0] \text{ s}^{-1}$. Fig. 8 shows the four 7×7 convolutional kernels learned using this input data, further referred to as the checkerboard dataset, and the aforementioned neural settings.

The effect of the scaling factor α on the neural response of this layer was exhaustively explored in [69]. As discussed, the lack of adaptation in the neuron model entails a high correlation between neural activity and the speed of the stimulus. The homeostasis parameter, through the correct value of α , mitigates this correlation for a wide range of speeds, thus achieving a constant postsynaptic firing rate that is independent of its presynaptic counterpart.

5.3 MS-Conv Layer: Local Motion Perception

MS-Conv is presented as a variation of the SS-Conv layer whose role is to provide motion estimates of the local features extracted in the latter by means of velocity-selective neurons. Similarly to feature identification, this selectivity emerges from visual experience through STDP.

As the basis of this formulation, the information required to perceive the motion of a particular feature is assumed to be exclusively contained in its corresponding presynaptic

neural map. Hence, contrary to those from the SS-Conv layer, convolutional kernels in MS-Conv are not connected to all presynaptic maps simultaneously. Instead, they are defined as $\mathbf{W}_k \in \mathbb{R}^{r^{l-1} \times m}$, and convolution is performed for each of these maps individually. This operation leads to kernels assigned to f^{l-1} feature-specific postsynaptic maps, among which the presynaptic weights (and weight updates) are shared. Since feature-specific activity is of minor importance for later stages of the architecture, the neural responses of these maps are merged into a single feature-invariant map per convolutional kernel. Per spatial location, postsynaptic spike trains are combined by prioritizing the firing of spikes over silent neurons. In this layer, the spatial dimensions of postsynaptic maps are halved through zero-padding and a convolutional stride of two pixels.

For the perception of local motion, we propose an augmentation of Eq. (8) based on the foundations of frequency-based optical flow methods [14] and bio-inspired motion detectors [60], [70]. Firstly, motion is to be extracted as orientation in the spatiotemporal domain. Therefore, neural connections in the MS-Conv layer are considered multisynaptic with different constant transmission delays as given by $\tau \in \mathbb{R}^m$. Secondly, since these delays (and the rest of neural parameters) are equal for all (spatiotemporal) convolutional kernels, inhibitory synapses are required to prevent the firing of erroneous postsynaptic spikes when the input trace only fits part of the excitatory component of the kernels. To account for this, each MS-Conv kernel is defined by a pair of excitatory and inhibitory plastic weight matrices, denoted by $\mathbf{W}_k^{\text{exc}}$ and $\mathbf{W}_k^{\text{inh}}$, respectively. According to these additions, the forcing function of cells in this layer is expressed as:

$$i_{i,k,ch}^l(t) = \sum_{j=1}^{r^{l-1}} \sum_{d=1}^m (W_{j,d,k}^{\text{exc}} + \beta W_{j,d,k}^{\text{inh}}) s_{j,ch}^{l-1}(t - \tau_d) - \max_{\forall b \in \mathcal{N}_{i,k,ch}} \sum_{j=1}^{r^{l-1}} \sum_{d=1}^m X_{b,j,d,ch}(t) \quad (9)$$

where β scales the impact of inhibitory synapses, and the presynaptic trace is defined as $\mathbf{X}_i \in \mathbb{R}^{r^{l-1} \times m \times f^{l-1}}$.

Due to the neural spatial disposition, the implementation of STDP in this layer is, in essence, identical to the one employed for SS-Conv. With respect to the learning of inhibitory kernels, the parameter a from Eq. (6) remains at 0, w_{init} is set to -0.5 , and the weights are initialized at 0. This discrepancy between w_{init} and the initialization weight enables neurons to be reactive to different input features until kernel specialization. With this configuration, after convergence, inhibitory weight distributions are naturally constrained in the range $\mathbf{W}_k^{\text{inh}} \in [-1, 0]$.

To evaluate the performance of the MS-Conv layer, sixteen (excitatory and inhibitory) 7×7 kernels were simultaneously trained using the pure horizontal and vertical stimuli from the checkerboard dataset. Neural parameters were empirically set to $v_{\text{th}} = 1.0$, $\lambda_v = \lambda_X = 5.0 \text{ ms}$, $\alpha = 0.25$, and $\beta = 0.75$; and the SS-Conv kernels in Fig. 8 were employed for feature extraction. With respect to the spatiotemporal characteristics of MS-Conv kernels, each multisynaptic connection was comprised of ten subsynapses with constant transmission delays linearly spaced

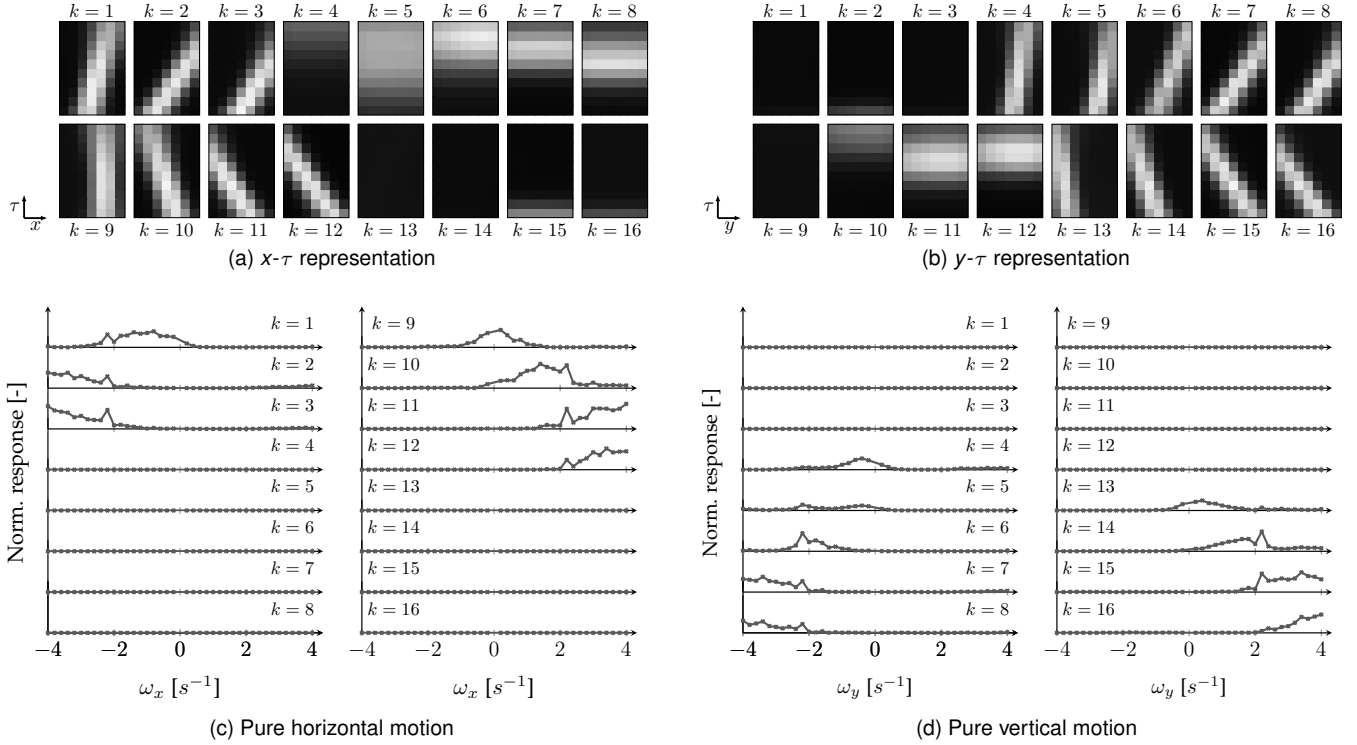


Fig. 9: Appearance (top) and neural response (bottom) of the sixteen $7 \times 7 \times 10$ MS-Conv kernels learned from the checkerboard dataset. Response plots are normalized by the maximum kernel response on the stimuli evaluated: 8.2763 spikes/ms by $k = 11$ for $\omega_x = 4.0 \text{ s}^{-1}$. Synaptic strength is encoded in color brightness: white for strong excitatory and weak inhibitory connections, and vice versa for black.

between 1.0 and 50.0 ms. Fig. 9 shows kernel appearance after convergence, and the response of the corresponding neural maps as a function of ω_x and ω_y .

This figure confirms that, with the MS-Conv connectivity pattern, STDP leads to the successful identification of the spatiotemporally-oriented traces of input features, and hence of their local motion. Out of the sixteen kernels trained, seven specialized to pure horizontal motion, and the remaining nine to pure vertical. Each direction of motion (up, down, left, and right) was captured by at least four kernels, which in turn were selective to a particular stimulus speed. For instance, upward motion was identified by kernels $k = 13$ – 16 , from slow to fast tuning speed. Therefore, kernels in this layer can be understood as local velocity-tuned filters that resemble those employed in frequency-based optical flow methods [14], [54], [55], [59]. However, instead of being manually designed, these filters emerge from visual experience in an unsupervised fashion.

In addition, remarkable is the fact that two of the (generally) four kernels that specialized to each of the aforementioned motion directions have overlapping neural responses despite the WTA mechanism. This is indicative of, first, a larger than sufficient number of kernels for this input dataset; and second and consequently, the relatively weak speed selectivity of neurons in this layer in comparison to their strong directional counterpart. Fig. 10 confirms these results through the evaluation of both selectivities as a function of β . This figure also corroborates the need for inhibition in MS-Conv kernels. A more extensive sensitivity analysis of these neural properties can be found in [69].

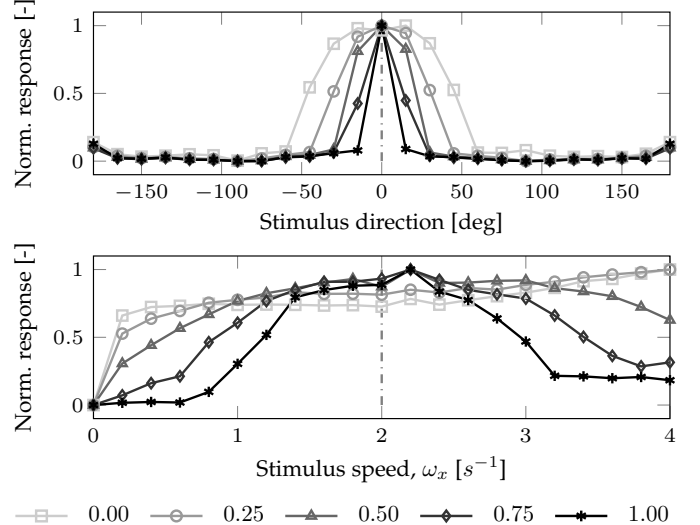


Fig. 10: Direction and speed selectivity of neurons in the MS-Conv layer as a function of β . The dashed lines indicate the training configuration, and each response plot is normalized by its maximum value.

5.4 Pooling Layer: From Local to Global

As an intermediate stage between the MS-Conv and Dense layers, the Pooling layer is employed in the SNN architecture as a means to reduce the spatial dimensionality of the former, and hence to facilitate the learning of the latter. The intuition of this layer is that, by pooling local motion estimates over large portions of the visual scene, a more accurate measure of the global motion in each of these

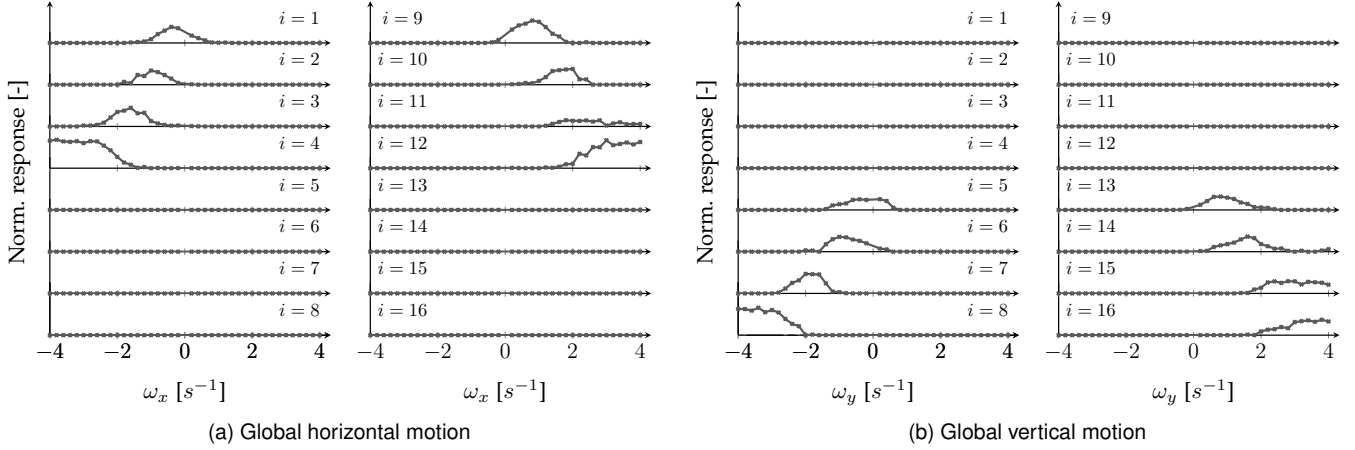


Fig. 11: Neural response of the sixteen individual neurons from the Dense layer trained in the checkerboard dataset. Response plots are normalized by the maximum neural response on the stimuli evaluated: 0.3 spikes/ms by $i = 4$ for $\omega_x = -3.8 \text{ s}^{-1}$.

regions can be obtained, thus mitigating the effect of the aperture problem.

Similarly to SS-Conv, the Pooling layer is convolutional and single-synaptic. The internal dynamics of its neurons is driven by the forcing function described in Eq. (8), but without the need for $N_{i,k}$ since presynaptic connections are not plastic. Instead, this layer is characterized by the same number of neural maps as the MS-Conv, each one assigned with an excitatory kernel W_k that has unitary weights with its presynaptic counterpart and null with the rest. In addition, the application of the WTA inhibitory mechanism is neglected, and there is no overlap between receptive fields. As shown in Fig. 5, we used 8×8 convolutional kernels in this layer, thus resulting in postsynaptic maps with 4×4 cells each. Further, neural parameters were empirically set to $v_{\text{th}} = 0.5$, $\lambda_v = \lambda_X = 5.0 \text{ ms}$, $\alpha = 0.15$, and $\tau = 1.0 \text{ ms}$.

5.5 Dense Layer: Global Motion Perception

The Dense layer, as the final stage of the SNN architecture, is comprised of individual neurons fully connected to cells in the Pooling layer via single-synaptic plastic connections. Similarly to final regions of biological visual motion systems [1], neurons in this layer develop selectivity to the global motion of the scene from visual experience through STDP.

With respect to implementation details, synaptic plasticity is conducted as described in Section 4, and the forcing function of Dense neurons resembles Eq. (4), but referring to the convolutional presynaptic layer to which these cells are connected. This expression is then defined as:

$$i_i^l(t) = \sum_{j=1}^{n^{l-1}} \sum_{ch=1}^{f^{l-1}} (W_{i,j,ch} s_{j,ch}^{l-1}(t - \tau) - X_{i,j,ch}(t)) \quad (10)$$

where the efficacy and trace of presynaptic connections are defined as $W_i \in \mathbb{R}^{n^{l-1} \times f^{l-1}}$ and $X_i \in \mathbb{R}^{n^{l-1} \times f^{l-1}}$, respectively.

To evaluate the performance, a Dense layer with sixteen individual neurons was trained as the final stage of a neural architecture comprised of the SS-Conv in Fig. 8 for feature

extraction, the MS-Conv in Fig. 9 for local motion perception, and a Pooling layer for spatial dimensionality reduction. Neural parameters were empirically set to $v_{\text{th}} = 0.5$, $\lambda_v = \lambda_X = 5.0 \text{ ms}$, $\alpha = 0.1$, and $\tau = 1.0 \text{ ms}$. Fig. 11 shows the neural response (after convergence) of cells in this layer as a function of ω_x and ω_y .

From this figure, neurons in the Dense layer are successful at capturing the dominant global motion pattern from the spatial distribution of local motion estimates from the previous layers. Out of the sixteen neurons trained, groups of four specialized to each motion direction, with different tuning speeds so as to cover the ventral flow range of the dataset, i.e. $\{\|\omega_x\|, \|\omega_y\|\} \in [0.2, 4.0] \text{ s}^{-1}$. Note that the direction and speed selectivity of these neurons is exclusively dependent on those of the spatiotemporal MS-Conv kernels.

In addition to this evaluation, Fig. 12 is shown to assess the activity of neurons from this layer in response to speed profiles that differ from the constant-speed sequences employed during training. Specifically, three different profiles of leftward horizontal motion were used in combination with the checkerboard texture. These sequences were characterized respectively by, first, constant-speed segments and step changes (see Fig. 12a); second, constant accelerations (see Fig. 12b); and third, a fluctuating acceleration (see Fig. 12c). Due to the pure leftward motion of the stimuli, only the activities of neurons specialized to this motion direction are shown, i.e. cells $i = 1-4$ from Fig. 11. Neural activity is measured through the postsynaptic trace $y_i(t)$ of these units, which, similarly to Eq. (2), keeps track of the recent history of postsynaptic spikes emitted by a particular neuron and is given by Eq. (11).

$$\lambda_y \frac{dy_i(t)}{dt} = -y_i(t) + s_i^l(t) \quad (11)$$

where $\lambda_y = 5.0 \text{ ms}$ to maintain consistency with the rest of the neural architecture.

Results in Fig. 12 confirm that, even though the network was trained using constant-speed stimuli, the spiking activity of neurons in the Dense layer can still be seen as indicative of the global motion of the visual scene in accelerated, or

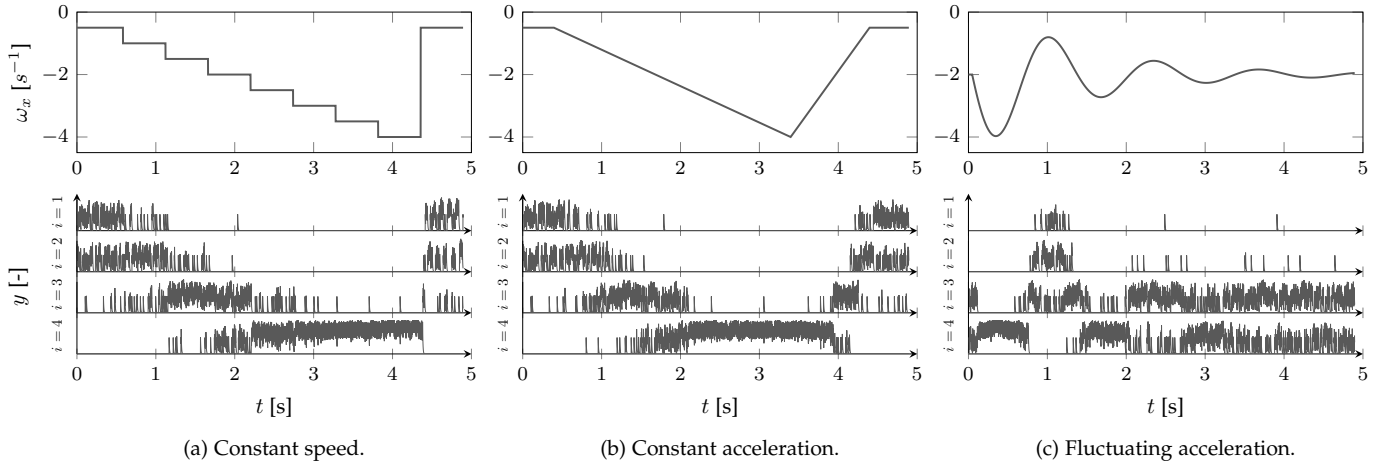


Fig. 12: Temporal course of the postsynaptic trace of neurons $i = 1\text{--}4$ from the Dense layer (bottom, see Fig. 11) in response to leftward input stimuli with different speed profiles (top) and from the checkerboard texture. Plots are normalized by the maximum trace on the stimuli evaluated: 0.4098 by $i = 4$ at $t = 0.36$ s for the fluctuating acceleration case.

with abrupt speed variations, sequences. Response aspects, such as the overlap of neural activity for some ventral flow ranges, or the dominance of $i = 4$ for fast motion, are in line with the selectivity of these neurons, as shown in Fig. 11a.

6 ESTIMATION OF VISUAL OBSERVABLES FROM SPIKE-BASED OPTICAL FLOW

The global motion identified in the previous section could potentially be exploited to facilitate biologically plausible optical-flow-based control, such as the landing of a flying robot [13], [71]. This could be done, for instance, using a reinforcement-based spiking learning mechanism [47], [48]. This is, however, beyond the scope of this paper. Instead, to demonstrate the potential of our results, we perform a read out of the Pooling layer and train a shallow ANN using supervised learning, in order to obtain continuous values as estimates of optical flow visual observables. Specifically, we learn the ventral flow components ω_x and ω_y .

The readout mechanism that we propose is a Multi-Layer Perceptron (MLP) network comprised of three hidden layers with 256, 128, and 32 Rectified Linear Units (ReLUs) respectively, and an output layer with two linear neurons. With respect to the input data, individual snapshots of the postsynaptic trace $y_i(t)$ of neurons in the Pooling layer are employed. Note that trace information is normalized to the maximum value of each snapshot.

For the performance assessment of the proposed MLP in the task of ventral flow estimation, the SNN trained in the checkerboard dataset (see Figs. 8 and 9) was used as backend network. Consistently, the visual stimulus employed in this evaluation were also generated by moving the simulated DVS [27] at a constant altitude of 0.5 m with respect to a (virtual) checkerboard surface, towards which it is facing with $\phi = \theta = 0.0$ deg. Further, we fixed sensor orientation with respect to the scene so that only vertical and horizontal edges were perceivable.

Two datasets were generated for this analysis. On the one hand, a training set comprised of approximately 22 000 snapshots was created by moving the DVS in straight trajectories of different motion directions and constant speeds,

TABLE 1
Evaluation Errors of the Readout Architecture

| r [m] | $\max(\omega)$ [s^{-1}] | ε_{ω_x} [s^{-1}] | | ε_{ω_y} [s^{-1}] | |
|---------|-------------------------------|---------------------------------------|---------------|---------------------------------------|---------------|
| | | Mean | Var | Mean | Var |
| 0.25 | 0.5237 | 0.1548 | 0.0190 | 0.1972 | 0.0182 |
| 0.50 | 1.0474 | 0.1954 | 0.0244 | 0.2106 | 0.0239 |
| 0.75 | 1.5711 | 0.1890 | 0.0234 | 0.2081 | 0.0245 |
| 1.00 | 2.0947 | 0.1808 | 0.0209 | 0.2135 | 0.0273 |
| 1.25 | 2.6184 | 0.1940 | 0.0278 | 0.2238 | 0.0309 |
| 1.50 | 3.1421 | 0.2292 | 0.0339 | 0.2315 | 0.0338 |
| 1.75 | 3.6658 | 0.2646 | 0.0515 | 0.2767 | 0.0573 |
| 2.00 | 4.1895 | 0.3099 | 0.0722 | 0.3506 | 0.0902 |

Mean absolute error and error variance of the readout architecture on the test set. Each circular trajectory is characterized by its radius and maximum absolute ventral flow. Values highlighted in bold correspond to the lowest of each column.

with $\{|\omega_x|, |\omega_y|\} \in [0.2, 4.5] \text{ } s^{-1}$. The MLP was trained on this data using the Adam optimization algorithm [72] with a constant learning rate of 1.0×10^{-4} and a batch size of 128 samples. On the other hand, snapshots were recorded throughout eight counterclockwise circular trajectories, of radii $r \in [0.25, 2.00]$ m and 6.0 s of duration, for the evaluation of the inference capabilities of the readout architecture. This dataset is further referred to as the test set, and its interests derives from a great number of unseen (ω_x, ω_y) combinations, the presence of sign changes, and a maximum ventral flow of $|\omega_x| = |\omega_y| = 4.2 \text{ } s^{-1}$. For both datasets, ground truth measurements were obtained through the formulation introduced in Section 3.

Fig. 13 shows the resulting estimates from the evaluation of the readout mechanism on the test dataset after convergence. From this figure, the proposed MLP is successful at mapping the spiking normal flow estimates to the desired ventral flow components. Despite of this, its performance is characterized by being relatively noisy, due to the underlying spiking nature of the data, and by saturating at high ventral flow values. Fig. 14 and Table 1 are included for the understanding the error variations with the magnitude of these parameters.

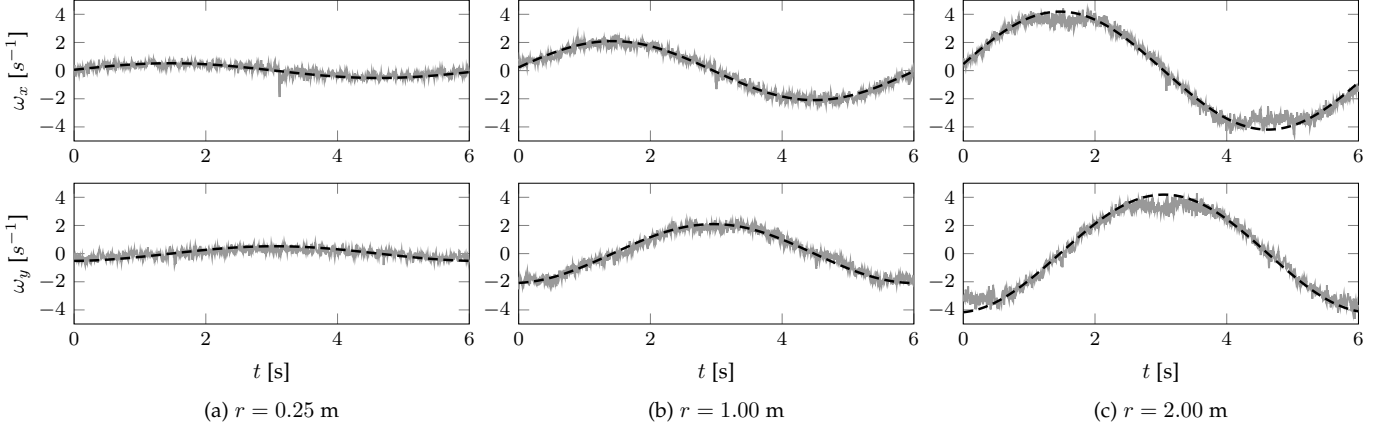


Fig. 13: Temporal evolution of the ventral flow components estimated with the readout architecture on three of the circular trajectories comprising the test set. Ground truth ventral flow measurements are shown through dashed black lines.

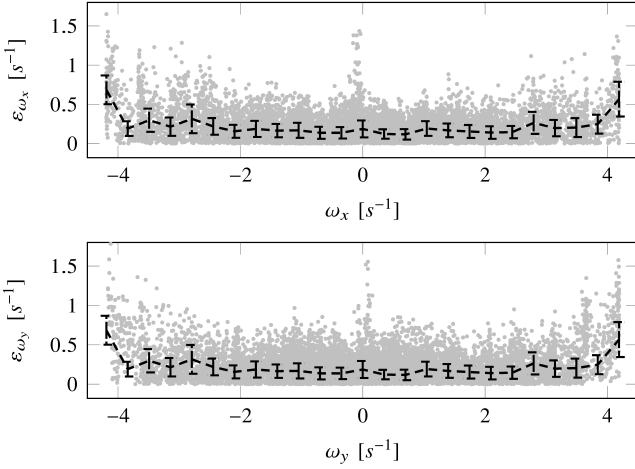


Fig. 14: Error distribution of the readout architecture on the test set. From top to bottom: Distribution of the absolute errors of ω_x and ω_y , and distribution of the normalized error of the mean absolute ventral flow $\hat{\omega}_{x,y}$. Measurements are depicted as gray dots, while the dashed black lines show the 25%, 50%, and 75% percentiles of the data.

Apart from the aforementioned performance limitations, these results show that, first, the absolute error is approximately constant $\{|\omega_x|, |\omega_y|\} < 2.5 \text{ s}^{-1}$; and second, this error increases for ventral flow components above this boundary value. Since the readout mechanism was trained on input stimuli with speeds of up to 4.5 s^{-1} , this poor performance is due to the SNN and the relatively weak speed selectivity of neurons in MS-Conv kernels at higher speeds. As shown in Fig. 9, for $\{|\omega_x|, |\omega_y|\} > 2.5 \text{ s}^{-1}$ (approximately), there is a consistent overlap between the neural responses of two kernels per perceivable (normal) flow direction, and consequently, the discernibility of different speeds is restricted. For a more accurate performance in this range, the checkerboard dataset used to train the SNN needs to be extended with higher ventral flow values, and the MS-Conv layer with additional kernels. Note that increasing the number of kernels without varying the training dataset would result in a further response overlap, and hence, no positive impact on the readout performance.

7 CONCLUSION

In this paper, we have presented the first hierarchical SNN architecture in which selectivity to the global motion of the visual scene emerges through STDP from the stimuli generated by an event-based vision sensor. The success of this emergence depends on three contributions. First, we show that an adaptive spiking neuron model is necessary to handle the rapidly varying input statistics of event-based sensors, and present a novel suitable formulation for this purpose. Second, we introduce a novel STDP implementation that, contrary to the current state-of-the-art of this learning protocol, is inherently stable. Third, the proposed SNN learns to perform a hierarchical feature extraction, effectively capturing geometric features, identifying the motion of these features, and integrating this information into a global ego-motion estimate. This is the first step in many towards highly effective visually aided micro robots.

APPENDIX

PROOF OF STABILITY OF MODIFIED STDP

We use Lyapunov theorem to investigate the global stability of the STDP implementation that we propose in this work. To simplify the proof, we assume that the neural connectivity is single-synaptic with $\tau = 0 \text{ ms}$. Using the STDP rule defined in Eqs. (5) and (6):

$$\Delta W_{i,j} = \eta \left(e^{-(W_{i,j} - w_{\text{init}})} (e^{\hat{X}_{i,j}} - a) - e^{(W_{i,j} - w_{\text{init}})} (e^{(1-\hat{X}_{i,j})} - a) \right) \quad (12)$$

Equilibrium weights $\bar{W}_{i,j}$ are given by $\Delta W_{i,j} = 0$:

$$\bar{W}_{i,j} = \frac{1}{2} \ln \left(\frac{e^{\hat{X}_{i,j}} - a}{e^{(1-\hat{X}_{i,j})} - a} \right) + w_{\text{init}} \quad (13)$$

If we let $z = W_{i,j} - \bar{W}_{i,j}$, Eq. (12) becomes:

$$\begin{aligned} \Delta W_{i,j} &= \eta (e^{\hat{X}_{i,j}} - a)^{\frac{1}{2}} (e^{(1-\hat{X}_{i,j})} - a)^{\frac{1}{2}} (e^{-z} - e^z) \\ \Delta W_{i,j} &= A(e^{-z} - e^z) \end{aligned} \quad (14)$$

where $A(\hat{X}_{i,j}, a)$ is a convenience function containing all components that are not a function of z .

Then we define the positive definite energy function $V(z) = \frac{1}{2}z^2$. As such, $\dot{V}(z)$ can be solved as follows:

$$\dot{V}(z) = z\dot{z} = z(\Delta W_{i,j} - \Delta \bar{W}_{i,j}) \quad (15)$$

where $\Delta \bar{W}_{i,j}$ can be computed from the time derivative of Eq. (13) as:

$$\Delta \bar{W}_{i,j} = \frac{1}{2} \Delta \hat{X}_{i,j} \left(\frac{e^{\hat{X}_{i,j}}}{e^{\hat{X}_{i,j}} - a} + \frac{e^{(1-\hat{X}_{i,j})}}{e^{(1-\hat{X}_{i,j})} - a} \right) \quad (16)$$

and $\Delta \hat{X}_{i,j}$ can be determined using Eq. (2):

$$\Delta \hat{X}_{i,j} = \frac{\alpha}{\lambda_X \hat{X}_{i,m}} (s_j^{l-1} - \hat{X}_{i,j} s_m^{l-1}) \quad (17)$$

where the subscript m denotes the index of the neuron with the maximum presynaptic trace.

Combining Eqs. (16) and (17) we are left with:

$$\begin{aligned} \Delta \bar{W}_{i,j} &= \frac{1}{2} \frac{\alpha}{\lambda_X \hat{X}_{i,m}} \left(\frac{e^{\hat{X}_{i,j}}}{e^{\hat{X}_{i,j}} - a} + \frac{e^{(1-\hat{X}_{i,j})}}{e^{(1-\hat{X}_{i,j})} - a} \right) \\ &\quad \cdot (s_j^{l-1} - \hat{X}_{i,j} s_m^{l-1}) \\ &= B(s_j^{l-1} - \hat{X}_{i,j} s_m^{l-1}) \end{aligned} \quad (18)$$

where $B(\hat{X}_{i,j}, a)$ is a convenience expression containing all elements not a function of s_j^{l-1} and s_m^{l-1} .

Now the energy derivative can be expressed simply as:

$$\dot{V}(z) = Az(e^{-z} - e^z) - Bz(s_j^{l-1} - \hat{X}_{i,j} s_m^{l-1}) \quad (19)$$

Using the Taylor expansion of e^z and e^{-z} we are left with:

$$\dot{V}(z) = -2A(z^2 + \frac{z^4}{3!} + \dots) - Bz(s_j^{l-1} - \hat{X}_{i,j} s_m^{l-1}) \quad (20)$$

Now if we look at the case where there is no external input to the neurons (i.e. the normalized presynaptic trace is constant, $s_j^{l-1} = s_m^{l-1} = 0$), we have that global asymptotic stability is guaranteed for $A > 0$, which can be ensured by setting $\eta > 0$ and $a < 1$.

When considering the input, we can define bounded error z with input-state stability inequality for a bounded input $u = \hat{X}_{i,j} s_m^{l-1} - s_j^{l-1}$:

$$\|z(t)\| \leq \beta(\|z(t)\|, t - t_0) + \gamma \left(\sup_{\tau \geq t_0} \|u(\tau)\| \right), \forall t \geq t_0 \quad (21)$$

where γ is the so-called Lyapunov gain will lead to input-state stability if positive definite.

Now, using the first order approximation for the Taylor expansion from (20), we can show:

$$\dot{V}(z) \leq -Az^2, \forall |z| \geq \frac{B(\hat{X}_{i,j} s_m^{l-1} - s_j^{l-1})}{2A} \quad (22)$$

with Lyapunov gain $\gamma = \frac{B}{2A}$.

As A must be positive for global asymptotic stability, for γ to be positive definite, B must also be positive. As such, λ_X and α must have the same sign. Additionally, the values of the constants in A and B can be used to control the bounds of the error z .

To give some physical meaning to these parameters we can see that adjusting a will change the sensitivity of

the STDP update to the presynaptic trace. The larger the difference $|1 - a|$, the less sensitive the update will be to the input. The time constant λ_X will adjust the rate at which the presynaptic trace is updated from the inputs s_j^{l-1} and s_m^{l-1} . The larger the time constant the slower the presynaptic trace will change and the more bounded the error will become. The scaling factor α changes the magnitude of the presynaptic trace and therefore the magnitude of the rate of change of the presynaptic trace.

One thing to note here is the discontinuity as $X_{i,m} \rightarrow 0$. This shows that the bound of the error can become large if the maximum presynaptic trace is small and the current neuron being updated is not the neuron with the maximum presynaptic trace. Physically this would mean that the network cannot accurately learn when the input is infinitively sparse. For the case where the input is measurably sparse, the learning can be improved by compensating with a larger time constant λ_X .

REFERENCES

- [1] A. Borst and M. Helmstaedter, "Common circuit design in fly and mammalian motion vision," *Nature Neuroscience*, vol. 18, no. 8, pp. 1067–1076, 2015.
- [2] J. J. Gibson, "The perception of the visual world," 1950.
- [3] M. V. Srinivasan, S. Zhang, M. Lehrer, and T. Collett, "Honeybee navigation en route to the goal: Visual flight control and odometry," *Journal of Experimental Biology*, vol. 199, no. 1, pp. 237–244, 1996.
- [4] F. Ruffier and N. Franceschini, "Optic flow regulation: The key to aircraft automatic guidance," *Robotics and Autonomous Systems*, vol. 50, no. 4, pp. 177–194, 2005.
- [5] E. Baird, N. Boeddeker, M. R. Ibbotson, and M. V. Srinivasan, "A universal strategy for visually guided landing," *Proceedings of the National Academy of Sciences*, vol. 110, no. 46, pp. 18 686–18 691, 2013.
- [6] C. De Wagter, S. Tijmons, B. D. W. Remes, and G. C. H. E. de Croon, "Autonomous flight of a 20-gram flapping wing MAV with a 4-gram onboard stereo vision system," in *Proceedings of the 2014 IEEE International Conference on Robotics and Automation*, 2014, pp. 4982–4987.
- [7] A. Kirkwood and M. F. Bear, "Hebbian synapses in visual cortex," *Journal of Neuroscience*, vol. 14, no. 3, pp. 1634–1645, 1994.
- [8] P. Lichtsteiner, C. Posch, and T. Delbrück, "A 128x128 120 dB 15 μ s latency asynchronous temporal contrast vision sensor," *IEEE Journal of Solid-State Circuits*, vol. 43, no. 2, pp. 566–576, 2008.
- [9] C. Posch, D. Matolin, and R. Wohlgemant, "A QVGA 143 dB dynamic range frame-free PWM image sensor with lossless pixel-level video compression and time-domain CDS," *IEEE Journal of Solid-State Circuits*, vol. 46, no. 1, pp. 259–275, 2011.
- [10] C. Brandli, R. Berner, M. Yang, S. Liu, and T. Delbrück, "A 240x180 130 dB 3 μ s latency global shutter spatiotemporal vision sensor," *IEEE Journal of Solid-State Circuits*, vol. 49, no. 10, pp. 2333–2341, 2014.
- [11] T. Delbrück and M. Lang, "Robotic goalie with 3 ms reaction time at 4% CPU load using event-based dynamic vision sensor," *Frontiers in Neuroscience*, vol. 7, pp. 1–7, 2013.
- [12] E. Mueggler, B. Huber, and D. Scaramuzza, "Event-based, 6-DOF pose tracking for high-speed maneuvers," in *Proceedings of the 2014 IEEE/RSJ International Conference on Intelligent Robots and Systems*, 2014, pp. 2761–2768.
- [13] B. J. P. Hordijk, K. Y. W. Schepers, and G. C. H. E. de Croon, "Vertical landing for micro air vehicles using event-based optical flow," *Journal of Field Robotics*, vol. 35, no. 1, pp. 69–90, 2018.
- [14] E. H. Adelson and J. R. Bergen, "Spatiotemporal energy models for the perception of motion," *Journal of the Optical Society of America*, vol. 2, no. 2, pp. 284–299, 1985.
- [15] R. Benosman, C. Clercq, X. Lagorce, S. Ieng, and C. Bartolozzi, "Event-based visual flow," *IEEE Transactions on Neural Networks and Learning Systems*, vol. 25, no. 2, pp. 407–417, 2014.

- [16] E. Ilg, N. Mayer, T. Saikia, M. Keuper, A. Dosovitskiy, and T. Brox, "Flownet 2.0: Evolution of optical flow estimation with deep networks," in *Proceedings of the 2017 IEEE Conference on Computer Vision and Pattern Recognition*, vol. 2, 2017, pp. 1647–1655.
- [17] W. Maass, "Networks of spiking neurons: The third generation of neural network models," *Neural Networks*, vol. 10, no. 9, pp. 1659–1671, 1997.
- [18] G. Orchard and R. Etienne-Cummings, "Bioinspired visual motion estimation," *Proceedings of the IEEE*, vol. 102, no. 10, pp. 1520–1536, 2014.
- [19] P. A. Merolla, J. V. Arthur, R. Alvarez-Icaza, A. S. Cassidy, J. Sawada, F. Akopyan, B. L. Jackson, N. Imam, C. Guo, Y. Nakamura *et al.*, "A million spiking-neuron integrated circuit with a scalable communication network and interface," *Science*, vol. 345, no. 6197, pp. 668–673, 2014.
- [20] M. Davies, N. Srinivasa, T.-H. Lin, G. Chinya, Y. Cao, S. H. Choday, G. Dimou, P. Joshi, N. Imam, S. Jain *et al.*, "Loihi: A neuromorphic manycore processor with on-chip learning," *IEEE Micro*, vol. 38, no. 1, pp. 82–99, 2018.
- [21] G. Q. Bi and M. M. Poo, "Synaptic modifications in cultured hippocampal neurons: Dependence on spike timing, synaptic strength, and postsynaptic cell type," *Journal of Neuroscience*, vol. 18, no. 24, pp. 10 464–10 472, 1998.
- [22] H. Markram, J. Lübke, M. Frotscher, and B. Sakmann, "Regulation of synaptic efficacy by coincidence of postsynaptic APs and EPSPs," *Science*, vol. 275, no. 5297, pp. 213–215, 1997.
- [23] T. Masquelier and S. J. Thorpe, "Unsupervised learning of visual features through spike timing dependent plasticity," *Public Library of Science: Computational Biology*, vol. 3, no. 2, pp. 247–257, 2007.
- [24] T. Iakymchuk, A. Rosado-Muñoz, J. F. Guerrero-Martínez, M. Bataller-Mompeán, and J. V. Francés-Villora, "Simplified spiking neural network architecture and STDP learning algorithm applied to image classification," *EURASIP Journal on Image and Video Processing*, vol. 2015, no. 1, pp. 1–11, 2015.
- [25] P. U. Diehl and M. Cook, "Unsupervised learning of digit recognition using spike-timing-dependent plasticity," *Frontiers in Computational Neuroscience*, vol. 9, pp. 1–9, 2015.
- [26] R. B. Stein, "A theoretical analysis of neuronal variability," *Biophysical Journal*, vol. 5, no. 2, pp. 173–194, 1965.
- [27] E. Mueggler, H. Rebecq, G. Gallego, T. Delbrück, and D. Scaramuzza, "The event-camera dataset and simulator: Event-based data for pose estimation, visual odometry, and SLAM," *The International Journal of Robotics Research*, vol. 36, no. 2, pp. 142–149, 2017.
- [28] A. L. Hodgkin and A. F. Huxley, "A quantitative description of membrane current and its application to conduction and excitation in nerve," *The Journal of Physiology*, vol. 117, no. 4, pp. 25–71, 1952.
- [29] E. M. Izhikevich, "Simple model of spiking neurons," *IEEE Transactions on Neural Networks*, vol. 14, no. 6, pp. 1569–1572, 2003.
- [30] W. M. Kistler, W. Gerstner, and J. L. van Hemmen, "Reduction of the Hodgkin-Huxley equations to a single-variable threshold model," *Neural Computation*, vol. 9, no. 5, pp. 1015–1045, 1997.
- [31] M. Baudry, "Synaptic plasticity and learning and memory: 15 years of progress," *Neurobiology of Learning and Memory*, vol. 70, no. 1, pp. 113–118, 1998.
- [32] K. Doya, "What are the computations of the cerebellum, the basal ganglia and the cerebral cortex?" *Neural Networks*, vol. 12, no. 7–8, pp. 961–974, 1999.
- [33] D. O. Hebb, *The organisation of behaviour: A neuropsychological theory*. Wiley, 1952.
- [34] H. Markram, W. Gerstner, and P. J. Sjöström, "Spike-timing-dependent plasticity: A comprehensive overview," *Frontiers in Synaptic Neuroscience*, vol. 4, pp. 1–3, 2012.
- [35] W. Gerstner and W. M. Kistler, *Spiking neuron models: Single neurons, populations, plasticity*. Cambridge University Press, 2002.
- [36] A. Tavanaei and A. S. Maida, "Multi-layer unsupervised learning in a spiking convolutional neural network," in *Proceedings of the 2017 IEEE International Joint Conference on Neural Networks*, 2017, pp. 2023–2030.
- [37] J. Sjöström and W. Gerstner, "Spike-timing dependent plasticity," *Frontiers in Neuroscience*, pp. 35–44, 2010.
- [38] M. C. W. Van Rossum, G. Q. Bi, and G. G. Turrigiano, "Stable Hebbian learning from spike timing-dependent plasticity," *Journal of Neuroscience*, vol. 20, no. 23, pp. 8812–8821, 2000.
- [39] A. Shrestha, K. Ahmed, Y. Wang, and Q. Qiu, "Stable spike-timing dependent plasticity rule for multilayer unsupervised and supervised learning," in *Proceedings of the 2017 International Joint Conference on Neural Networks*. IEEE, 2017, pp. 1999–2006.
- [40] S. M. Bohte, J. N. Kok, and H. La Poutré, "Error-backpropagation in temporally encoded networks of spiking neurons," *Neurocomputing*, vol. 48, no. 1, pp. 17–37, 2002.
- [41] A. Taherkhani, A. Belatreche, Y. Li, and L. P. Maguire, "A supervised learning algorithm for learning precise timing of multiple spikes in multilayer spiking neural networks," *IEEE Transactions on Neural Networks and Learning Systems*, pp. 1–14, 2018.
- [42] J. A. Pérez-Carrasco, B. Zhao, C. Serrano, B. Acha, T. Serrano-Gotarredona, S. Chen, and B. Linares-Barranco, "Mapping from frame-driven to frame-free event-driven vision systems by low-rate rate coding and coincidence processing—application to feed-forward convnets," *IEEE Transactions on Pattern Analysis and Machine Intelligence*, vol. 35, no. 11, pp. 2706–2719, 2013.
- [43] D. Zambrano, R. Nusselder, H. S. Scholte, and S. M. Bohte, "Efficient computation in adaptive artificial spiking neural networks," 2017. [Online]. Available: <https://arxiv.org/abs/1710.04838>
- [44] R. Van Rullen and S. J. Thorpe, "Rate coding versus temporal order coding: What the retinal ganglion cells tell the visual cortex," *Neural Computation*, vol. 13, no. 6, pp. 1255–1283, 2001.
- [45] R. V. Florian, "Reinforcement learning through modulation of spike-timing-dependent synaptic plasticity," *Neural Computation*, vol. 19, no. 6, pp. 1468–1502, 2007.
- [46] E. M. Izhikevich, "Solving the distal reward problem through linkage of STDP and dopamine signaling," *Cerebral Cortex*, vol. 17, no. 10, pp. 2443–2452, 2007.
- [47] J. O. Rombouts, P. R. Roelfsema, and S. M. Bohte, "Neurally plausible reinforcement learning of working memory tasks," in *Advances in Neural Information Processing Systems*, 2012, pp. 1871–1879.
- [48] J. O. Rombouts, A. van Ooyen, P. R. Roelfsema, and S. M. Bohte, "Biologically plausible multi-dimensional reinforcement learning in neural networks," in *International Conference on Artificial Neural Networks*, 2012, pp. 443–450.
- [49] J. Friedrich and M. Lengyel, "Goal-directed decision making with spiking neurons," *Journal of Neuroscience*, vol. 36, no. 5, pp. 1529–1546, 2016.
- [50] M. Mozaafari, M. Ganjtabesh, A. Nowzari-Dalini, S. J. Thorpe, and T. Masquelier, "Combining STDP and reward-modulated STDP in deep convolutional spiking neural networks for digit recognition," 2018. [Online]. Available: <https://arxiv.org/abs/1804.00227>
- [51] H. C. Longuet-Higgins and K. Prazdny, "The interpretation of a moving retinal image," *Proceedings of the Royal Society of London B: Biological Sciences*, vol. 208, no. 1173, pp. 385–397, 1980.
- [52] B. D. Lucas and T. Kanade, "An iterative technique of image registration and its application to stereo," in *Proceedings of the 7th International Joint Conference on Artificial Intelligence*, vol. 2, 1981, pp. 674–679.
- [53] R. Benosman, S. Ieng, C. Clercq, C. Bartolozzi, and M. Srinivasan, "Asynchronous frameless event-based optical flow," *Neural Networks*, vol. 27, pp. 32–37, 2012.
- [54] T. Brosch, S. Tschechne, and H. Neumann, "On event-based optical flow detection," *Frontiers in Neuroscience*, vol. 9, pp. 1–15, 2015.
- [55] S. Tschechne, R. Sailer, and H. Neumann, "Bio-inspired optic flow from event-based neuromorphic sensor input," in *Proceedings of the 6th IAPR Workshop on Artificial Neural Networks in Pattern Recognition*. Springer, 2014, pp. 171–182.
- [56] T. Brosch and H. Neumann, "Event-based optical flow on neuromorphic hardware," in *Proceedings of the 9th EAI International Conference on Bio-inspired Information and Communications Technologies*, 2016, pp. 551–558.
- [57] M. Giulioni, X. Lagorce, F. Galluppi, and R. B. Benosman, "Event-based computation of motion flow on a neuromorphic analog neural platform," *Frontiers in Neuroscience*, vol. 10, pp. 1–13, 2016.
- [58] C. Richter, F. Röhrbein, and J. Conradt, "Bio-inspired optic flow detection using neuromorphic hardware," *Bernstein Conference on Computational Neuroscience*, 2014, poster.
- [59] G. Orchard, R. Benosman, R. Etienne-Cummings, and N. V. Thakor, "A spiking neural network architecture for visual motion estimation," in *Proceedings of the 2013 IEEE Biomedical Circuits and Systems Conference*, 2013, pp. 298–301.
- [60] W. Reichardt, "Autocorrelation, a principle for the evaluation of sensory information by the central nervous system," *Sensory Communication*, pp. 303–317, 1961.
- [61] S. Ullman, *The interpretation of visual motion*. MIT Press, 1979.

- [62] A. P. Shon, R. P. Rao, and T. J. Sejnowski, "Motion detection and prediction through spike-timing dependent plasticity," *Network: Computation in Neural Systems*, vol. 15, no. 3, pp. 179–198, 2004.
- [63] O. G. Wenisch, J. Noll, and J. L. Van Hemmen, "Spontaneously emerging direction selectivity maps in visual cortex through STDP," *Biological Cybernetics*, vol. 93, no. 4, pp. 239–247, 2005.
- [64] S. V. Adams and C. M. Harris, "A computational model of innate directional selectivity refined by visual experience," *Scientific Reports*, vol. 5, pp. 1–13, 2015.
- [65] A. Morrison, A. Aertsen, and M. Diesmann, "Spike-timing-dependent plasticity in balanced random networks," *Neural Computation*, vol. 19, no. 6, pp. 1437–1467, 2007.
- [66] M. Abercrombie, C. J. Hickman, and M. L. Johnson, *A dictionary of biology*. Routledge, 2017.
- [67] S. M. Bohte, "Efficient spike-coding with multiplicative adaptation in a spike response model," in *Advances in Neural Information Processing Systems*, 2012, pp. 1835–1843.
- [68] S. J. Thorpe, "Spike arrival times: A highly efficient coding scheme for neural networks," *Parallel Processing in Neural Systems*, pp. 91–94, 1990.
- [69] F. Paredes-Valles, *Neuromorphic Computing of Event-Based Data for High-Speed Vision-Based Navigation*. M.Sc. Thesis, Faculty of Aerospace Engineering, Delft University of Technology, 2018. [Online]. Available: TU Delft Education Repository.
- [70] H. B. Barlow and W. R. Levick, "The mechanism of directionally selective units in rabbit's retina." *The Journal of Physiology*, vol. 178, no. 3, pp. 477–504, 1965.
- [71] H. Ho, C. De Wagter, B. D. W. Remes, and G. C. H. E. de Croon, "Optical-flow based self-supervised learning of obstacle appearance applied to MAV landing," *Robotics and Autonomous Systems*, vol. 100, pp. 78–94, 2018.
- [72] D. Kingma and J. Ba, "Adam: A method for stochastic optimization," 2014. [Online]. Available: <https://arxiv.org/abs/1412.6980>



Guido C. H. E. de Croon received his M.Sc. and Ph.D. in the field of Artificial Intelligence at Maastricht University, the Netherlands. His research interest lies with computationally efficient algorithms for robot autonomy, with an emphasis on computer vision. Since 2008 he has worked on algorithms for achieving autonomous flight with small and light-weight flying robots, such as the DelFly flapping wing MAV. In 2011–2012, he was a research fellow in the Advanced Concepts Team of the European Space Agency, where he

studied topics such as optical flow based control algorithms for extraterrestrial landing scenarios. Currently, he is associate professor at Delft University of Technology, the Netherlands, where he is the scientific lead of the Micro Air Vehicle Laboratory.



Federico Paredes-Vallés received his B.Sc. in Aerospace Engineering from the Polytechnic University of Valencia, Spain, in 2015, and his M.Sc. from Delft University of Technology, the Netherlands, in 2018. He is currently a Ph.D. candidate in the Micro Air Vehicle Laboratory at the latter university. His research interest is the intersection of machine learning, neuroscience, computer vision, and aerial robotics.



Kirk Y. W. Schepers received his M.Sc. from the Faculty of Aerospace Engineering at Delft University of Technology, the Netherlands, in 2014. Since then, he has been a Ph.D. candidate in the Micro Air Vehicle Laboratory at the same university. His research focuses on the development of embedded software which facilitates high level autonomy of micro air vehicles. His work is mainly in the fields of evolutionary robotics, embodied cognition, and vision-based navigation.